Geophysical Research Letters

RESEARCH LETTER
10.1029/2024GL111460

Key Points:

- Directivities of 31 M_L 3.5–5.7 earthquakes along the Marmara seismic gap were estimated from apparent source-time function variations
- 72% of strongly asymmetric earthquakes show directivity toward the east, implying higher ground motions toward the Istanbul region
- The rupture directivities are consistent with right-lateral east–west trending source mechanisms at the Main Marmara Fault

Supporting Information:

Supporting Information may be found in the online version of this article.

Correspondence to:
P. Martínez-Garzón,
patricia@gfz-potsdam.de

Citation:
Chen, X., Martínez-Garzón, P., Kwiatek, G., Ben-Zion, Y., Bohnhoff, M., & Cotton, F. (2025). Rupture directivity of moderate earthquakes along the main Marmara fault suggests larger ground motion toward Istanbul. *Geophysical Research Letters*, *52*, e2024GL111460. https://doi.org/10.1029/2024GL111460

Received 22 JUL 2024
Accepted 15 NOV 2024

Rupture Directivity of Moderate Earthquakes Along the Main Marmara Fault Suggests Larger Ground Motion Towards Istanbul

Xiang Chen[1], Patricia Martínez-Garzón[1], Grzegorz Kwiatek[1], Yehuda Ben-Zion[2,3], Marco Bohnhoff[1,4], and Fabrice Cotton[1,5]

[1]Helmholtz Centre Potsdam GFZ German Research Centre for Geosciences, Potsdam, Germany, [2]Department of Earth Sciences, University of Southern California, Los Angeles, CA, USA, [3]Statewide California Earthquake Center, University of Southern California, Los Angeles, CA, USA, [4]Institute of Geological Sciences, Free University Berlin, Berlin, Germany, [5]Institute of Geosciences, University of Potsdam, Potsdam, Germany

Abstract Analysis of earthquake rupture directivity provides key information for seismic hazard and risk assessment, particularly for faults near urban areas. We analyze directivity patterns for 31 well-constrained $M_L \geq 3.5$ earthquakes along the Main Marmara Fault, in direct proximity to Istanbul. We calculate source mechanisms with a waveform modeling approach and analyze earthquake directivity from apparent source-time functions using empirical Green's functions. Most of the strike-slip earthquakes to the west of the Princes Islands segment display a predominantly asymmetric rupture toward the east with the median directivity trending 85°, consistent with the Main Marmara Fault strike. Consequently, earthquake ground shaking may be more pronounced toward Istanbul. This holds potentially for a large earthquake on the Main Marmara Fault which is late in its seismic cycle. Our results motivate the importance of evaluating the impact of eastward asymmetric ruptures on the probabilistic seismic hazard and risk assessment around Istanbul.

Plain Language Summary Analyzing how earthquakes release the accumulated strain energy in space can help us understand the resulting shaking in particular locations. We studied 31 earthquakes with magnitudes $M_L \geq 3.5$ that occurred along the North Anatolian Fault in the Marmara region near Istanbul, northwestern Türkiye. We derived orientations of fault planes using focal-mechanism inversion, as well as the direction in which the seismic energy release is focused (rupture directivity). We find that most of the analyzed earthquakes display strike-slip movement, matching the orientation of the GPS-derived deformation field in this area, which is different from previous studies proposing dominantly normal faulting kinematics, particularly on the western part of the Main Marmara Fault. We also find that earthquakes to the west of the Princes Islands south of Istanbul radiate seismic energy mostly toward the east. This also suggests that the ground shaking from the earthquakes could be stronger toward Istanbul and weaker in the opposite direction. Our findings show that it is important to consider how earthquake ruptures propagate when evaluating the earthquake risk, especially near urban areas.

1. Introduction

Earthquake rupture directivity is an important factor controlling the spatial distribution of seismic ground motions. As such, determining how earthquakes propagate provides key information for regional seismic hazard estimates and subsequent risk assessments. For example, for unilateral or strongly asymmetric ruptures, significantly larger ground motion amplitudes of the seismic waves are expected in the direction of rupture propagation, and consequently reduced ground motions in the opposite direction.

Depending on the available seismic network, rupture directivity can be calculated for moderate to large earthquakes with magnitudes M > 4.5 (e.g., Calderoni et al., 2015; Seekins & Boatwright, 2010; Venkataraman & Kanamori, 2004) as well as for smaller earthquakes (e.g., Boatwright, 2007; Holmgren et al., 2023; Kurzon et al., 2014; López-Comino et al., 2021; Seo et al., 2022). Multiple techniques have been employed to resolve rupture directivity by deconvolving propagation effects using synthetic (e.g., Tinti et al., 2016) and empirical (e.g., Calderoni et al., 2023; Tan & Helmberger, 2010) Green's functions. Other methods incorporate measuring relative differences between centroid and hypocenter location (He et al., 2015), analysis of second seismic moments (e.g., McGuire, 2004; Meng et al., 2020), or direct analysis of observed ground motions (Boatwright & Boore, 1982; Chen et al., 2014; Colavitti et al., 2022; Türker et al., 2022).

Despite difficulties associated with the higher frequencies and lower signal-to-noise ratio, some studies have shown that small to moderate events display a preferred rupture direction that is likely governed by particular mechanisms (Kane et al., 2013; Wang & Rubin, 2011), which may be diverse. Previous studies suggested that unilateral or strongly asymmetric earthquake ruptures and associated directivity effects are related to variations in fault geometry (e.g., Calderoni et al., 2015, 2017; Kurzon et al., 2014; Zhang et al., 2023), stress and/or strength gradients along the fault (Yoshida et al., 2019), and ruptures on bimaterial faults (e.g., Calderoni et al., 2015; Kurzon et al., 2014; Lengliné & Got, 2011; Meng et al., 2020).

Resolving directivity of well-recorded moderate and (more frequent) small events across sections of continental strike-slip faults can contribute to identifying regions of increased earthquake ground motions. A long-standing question is whether the directivity of large events is consistent with that of smaller events. If this is the case, rupture directivity of smaller events could contribute to predicting the spatial variations of ground motions in a target region in case of large future earthquakes. This is particularly important for estimating seismic hazard and subsequent risk of urban areas near transform faults, for example, in the Istanbul metropolitan region, or near Los Angeles and the San Francisco Bay area.

The Marmara section in northwestern Türkiye is the only portion of the entire North Anatolian Fault Zone (NAFZ) in Türkiye that has not generated a large ($M > 7$) earthquake since 1766. At an average recurrence rate of 250 years (Ambraseys, 2002; Bohnhoff et al., 2016; Murru et al., 2016), it is late in its seismic cycle. The main NAFZ branch runs below the Sea of Marmara (Main Marmara Fault, MMF) and is located less than 20 km away from the Istanbul metropolis with >16 million inhabitants (Figure 1a). Therefore, quantifying the seismic hazard in this region is of uttermost importance for assessing the resulting seismic risk. The eastern part of the MMF (the Princes Islands segment) immediately south of Istanbul is locked, representing a potential segment to rupture in the pending large earthquake (Bohnhoff et al., 2013; Ergintav et al., 2014). In contrast, the western part of the MMF is creeping to a substantial extent based on observations from seafloor geodesy (Yamamoto et al., 2019) and the occurrence of earthquake repeaters (Becker et al., 2023a; Bohnhoff, Wollin, et al., 2017). The central segment in between likely is in an intermediate status (Becker et al., 2023a) and locked toward the east (Lange et al., 2019) (Figure 1).

Despite the high relevance of the MMF, there are no systematic studies quantifying earthquake rupture directivity in the Marmara region. Directivity studies focused mainly on the 1999 $M > 7$ Izmit and Düzce earthquakes and the 2022 M_w 6.0 Düzce earthquake to the east of the Sea of Marmara and reported on a preferred rupture propagation toward the east (e.g., Martínez-Garzón et al., 2023; Tibi et al., 2001; Türker et al., 2023). Along the MMF, an eastward rupture directivity was resolved for the largest three events in the 2019 M_L 5.7 Silivri sequence by analyzing the amplitude of ground motions (Türker et al., 2022).

The data availability and seismic network coverage have been substantially improved in recent years by combining recordings from different national networks (Becker et al., 2023a, 2023b; Wollin et al., 2018) and GONAF borehole seismometers (Bohnhoff, Dresen, et al., 2017; Malin et al., 2018). Taking advantage of these improvements in monitoring conditions, we calculate the source mechanisms and the rupture directivities of 31 best-recorded $3.5 \leq M_L \leq 5.7$ earthquakes located on or near the submarine MMF. The source parameters from these events are then employed to evaluate common patterns at different fault segments and with respect to their rupture kinematics.

2. Data and Method

The employed earthquake catalog spans the time period from 2006 to 2020 and includes a total of 13,812 events (Becker et al., 2023a; Wollin et al., 2018). From the catalog, there are 68 $M_L \geq 3.5$ earthquakes occurring on and around the MMF (Figure 1). We use broadband seismic recordings from regional stations (see Open Research). In total, we employ waveform recordings from 88 seismic stations with epicentral distances ranging from 35 to 224 km, resulting in take-off angles ranging from 47 to 105° and assuming a 1-D velocity model (Durand et al., 2020; Karabulut et al., 2011).

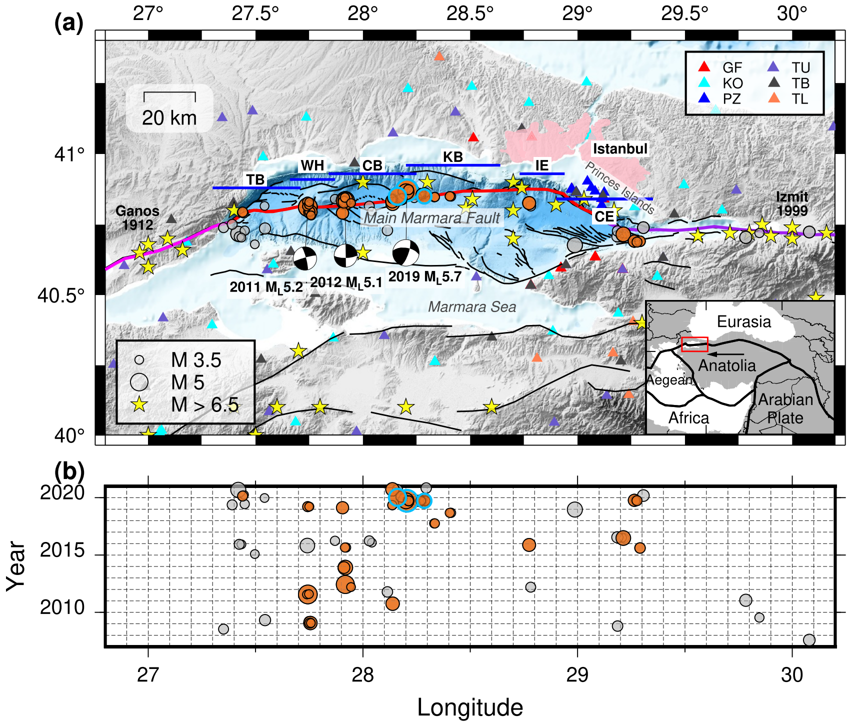

Figure 1. Seismotectonics of the Marmara region and analyzed earthquakes. Gray and orange dots show $M_L \geq 3.5$ earthquakes in 2006–2020 and those selected for directivity assessment, respectively. (a) Spatial distribution of M_L 3.5 seismicity. Yellow stars mark historical $M > 6.5$ earthquakes within the last 2000 years (Ambraseys, 2002; Bohnhoff et al., 2016; Parsons, 2004). Thick lines show ruptured portions of the 1912 M_w 7.4 Ganos (magenta) and the 1999 M_w 7.4 Izmit (purple) earthquakes, as well as the MMF (red). Blue horizontal lines indicate the along-fault segments of the MMF: TB (Tekirdağ Basin), WH (Western High), CB (Central Basin), KB (Kumburgaz Basin), IE (Istanbul East), and CE (Cinarcik East). Triangles indicate selected seismic stations. Source mechanisms (this study) are shown for $M \geq 5$ earthquakes. Lower right inset: Broader tectonic map of the study region. (b) Longitude versus time distribution of the earthquakes. The three earthquakes shown in Figure 2 are circled with cyan edge color.

2.1. Source Mechanism Determination

To resolve the fault geometry and kinematics of the analyzed events with M_L 3.5–5.7, we determined earthquake source mechanisms using the Cut and Paste (CAP) approach (Zhao & Helmberger, 1994; Zhu & Helmberger, 1996). In the CAP method, the seismograms are transferred into radial, tangential and vertical components and decomposed into the P-wave and surface-wave segments. These different wave segments are fit separately, allowing a time shift between the observed and synthetic waveforms due to the velocity model imperfections and crust lateral heterogeneities. The theoretical Green's functions and synthetic seismograms were calculated using the frequency-number algorithm (Wang & Herrmann, 1980; Zhu & Rivera, 2002) assuming 1-D velocity model (Durand et al., 2020; Karabulut et al., 2011). Detailed processing procedures are shown in Text S1 of Supporting Information S1. Three examples of focal mechanisms resolved with the CAP method are shown in Figures 2b–2d.

2.2. Empirical Green's Function Deconvolution

The earthquake directivity effects are here investigated utilizing the azimuthal variations of the apparent source-time functions (ASTFs) using empirical Green's function (EGF) technique (Hartzell, 1978). EGF deconvolution has been found to be an effective method in isolating the earthquake source term from seismograms (Abercrombie et al., 2017; Kwiatek, 2008; Prieto et al., 2004). The underlying assumption of the EGF method is that the smaller earthquake that occurred near the target event and displayed a similar focal mechanism can be considered an approximation of the Green's function and used to remove the propagation and site effects from the target event. Further details on EGF selection criteria and deconvolution procedure are provided in the Text S2 of Supporting Information S1. Out of the 68 $M_L \geq 3.5$ earthquakes, 50 target events were found to have EGFs according to the

10.1029/2024GL111460

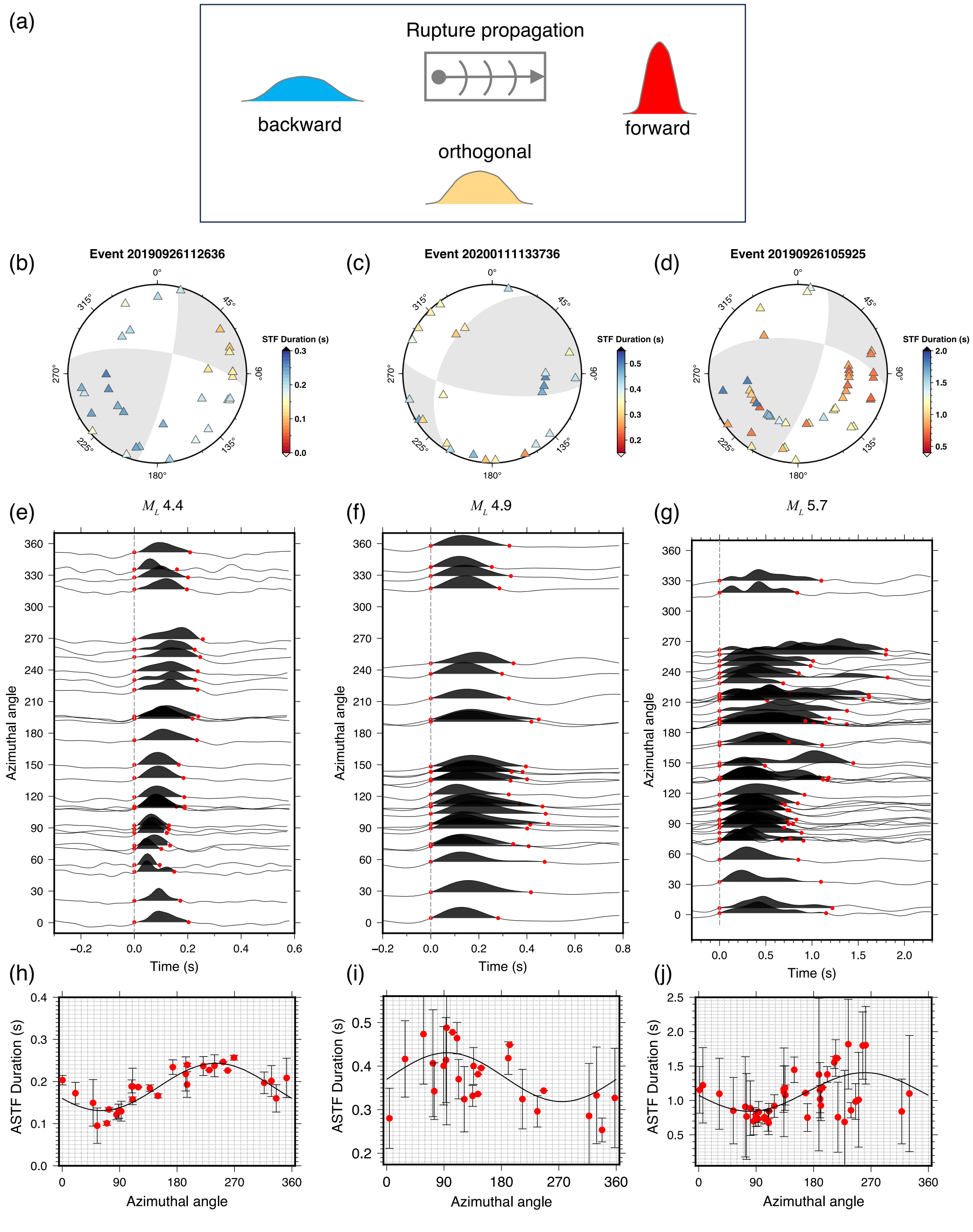

Figure 2. Schematic illustration of rupture directivity and examples of ASTFs and earthquake rupture directivity resolved for three earthquakes. (a) Sketch showing the directivity effect on the ASTFs at different azimuths. (b) Source mechanisms with projected seismic stations (triangles) used for ASTF analysis on the lower hemisphere of the focal sphere for a M_L 4.4 event (ID 20190926112636). Color coding indicates the ASTF duration. (c) Same as panel b but for event M_L 4.9 with ID 20200111133736. (d) Same as panel b but for event M_L 5.7 with ID 20190926105925. (e–g) ASTFs at different azimuths for the events. Red dots mark the starts and ends of the ASTFs. (h–j) ASTF durations (red) and the best-fitting unilateral rupture models (black curves). Error bars show standard deviations of ASTF durations from EGFs. The larger uncertainties in the ASTF duration of the M_L 5.7 earthquake are due to estimates from the larger number of EGF events used as well as the more complex rupture pattern (see Turhan, Acarel et al., 2023).

criterio selection above. The EGF number varies for each station in each target event, ranging from a single EGF up to 27 EGFs in the 2019 M_L 5.7 earthquake. The durations of resulting stacked ASTFs observable at different azimuths (cf. Figures 2e–2g) were automatically calculated from stacked ASTFs with reference to the baseline.

The duration uncertainty for a particular station was estimated as the standard deviation of ASTF durations if multiple EGFs were available.

2.3. Constraining Rupture Directivity

For strike-slip faulting with rupture propagation coinciding with the slip vector, earthquake rupture direction should predominantly lead to azimuthal variations in the observed ASTFs and related ground motions. For a unilateral rupture representing an end-member case, the ASTFs show shorter duration and higher amplitude in the forward direction of earthquake rupture, and longer duration and lower amplitude in the backward rupture direction (Figure 2a). The duration of the ASTF observed at a station for the case of a pure unilateral pulse-type rupture could be described as a function of azimuth (Ben-Menahem & Singh, 1981):

$$T(\theta) = \frac{L}{V_r} - \frac{L\cos\theta}{V_S}, \tag{1}$$

where T is the ASTF duration, θ refers to the azimuth angle between the earthquake source and seismic station, L is the earthquake rupture length, V_r indicates the rupture velocity, and V_S denotes the S-wave velocity (here set to $V_S = 3.56$ km/s at 10 km depth for the assumed velocity model Karabulut et al., 2011). We then performed an exhaustive search over the space of model parameters ($\theta \in [0, 360]°$, $L \in [0.1, 20]$ km and $V_r \in [10\%\ V_S, 100\%\ V_S]$) and tested which particular combination of (θ, L, V_r) led to the best fit between the model (Equation 1) and observed durations. Each event has at least 8 independent ASTF observations stacked from multiple EGFs. The minimized cost function that is the sum of point-to-curve distances (cf. Figures 2h–2j) normalized by the number of stations. We further applied an evaluation of the unilateral fitting results by conducting the two-sample t-test (Text S2 in Supporting Information S1) for the ASTF durations in the estimated forward and backward directions. For events not passing the t-test, we additionally explored the fit to bilateral and asymmetrical bilateral models (Cesca et al., 2011):

$$T(\theta) = \max\left[\frac{L(1-\chi)}{V_r} - \frac{L(1-\chi)\cos\theta}{V_S}, \frac{\chi L}{V_r} - \frac{\chi L\cos\theta}{V_S}\right], \tag{2}$$

in which the model contains two unilateral ruptures $[L(1-\chi), \chi L]$ with opposite directions, and the χ is a directivity coefficient in the range of [0,0.5]. When $\chi = 0$, Equation 2 is equivalent to Equation 1 representing a pure unilateral rupture, while when $\chi = 0.5$ Equation 2 indicates a pure bilateral rupture.

3. Results

3.1. Predominance of Strike-Slip Kinematics From Source Mechanisms

We obtained source mechanisms for 31 $M_L \geq 3.5$ events on and around the MMF, out of which 29 show a predominant strike-slip mechanism (fault parameters provided in Table S1 of Supporting Information S1). Figure 3 shows representative examples of two inverted source mechanisms in which 16 and 32 stations were employed for the inversions.

The observed predominance of strike-slip kinematics along the fault differs from some previous studies in this region, which obtained normal-faulting kinematics in the western part of the MMF inverting first-motion polarities (e.g., Öztürk et al., 2015; Wollin et al., 2018, 2019). The waveform-based source mechanisms from the CAP method are likely more stable than those from first-motion polarities, and they are more consistent with strike-slip activity along the fault. This observation might also be partially driven by the fact that we focused on the largest events in the region ($M_L \geq 3.5$), which are more likely to occur on the main fault trace. The inverted moment magnitudes for these events agree with those from the catalog (M_L) and those from a spectral fitting method used in a separate study (Chen, Kwiatek, et al., 2024) (Figure S1 in Supporting Information S1).

Based on the spatial distribution of earthquakes we grouped our source mechanisms into 4 clusters according to their corresponding fault regions (see Figure 4a). In the Western High (WH), 4 earthquakes display strike-slip kinematics, three of which have north-east striking nodal planes at 72 ± 3° NE, likely representing the actual fault plane inline with the MMF. In the western edge of the Central Basin (CBw), the data consist of 5 consistent

10.1029/2024GL111460

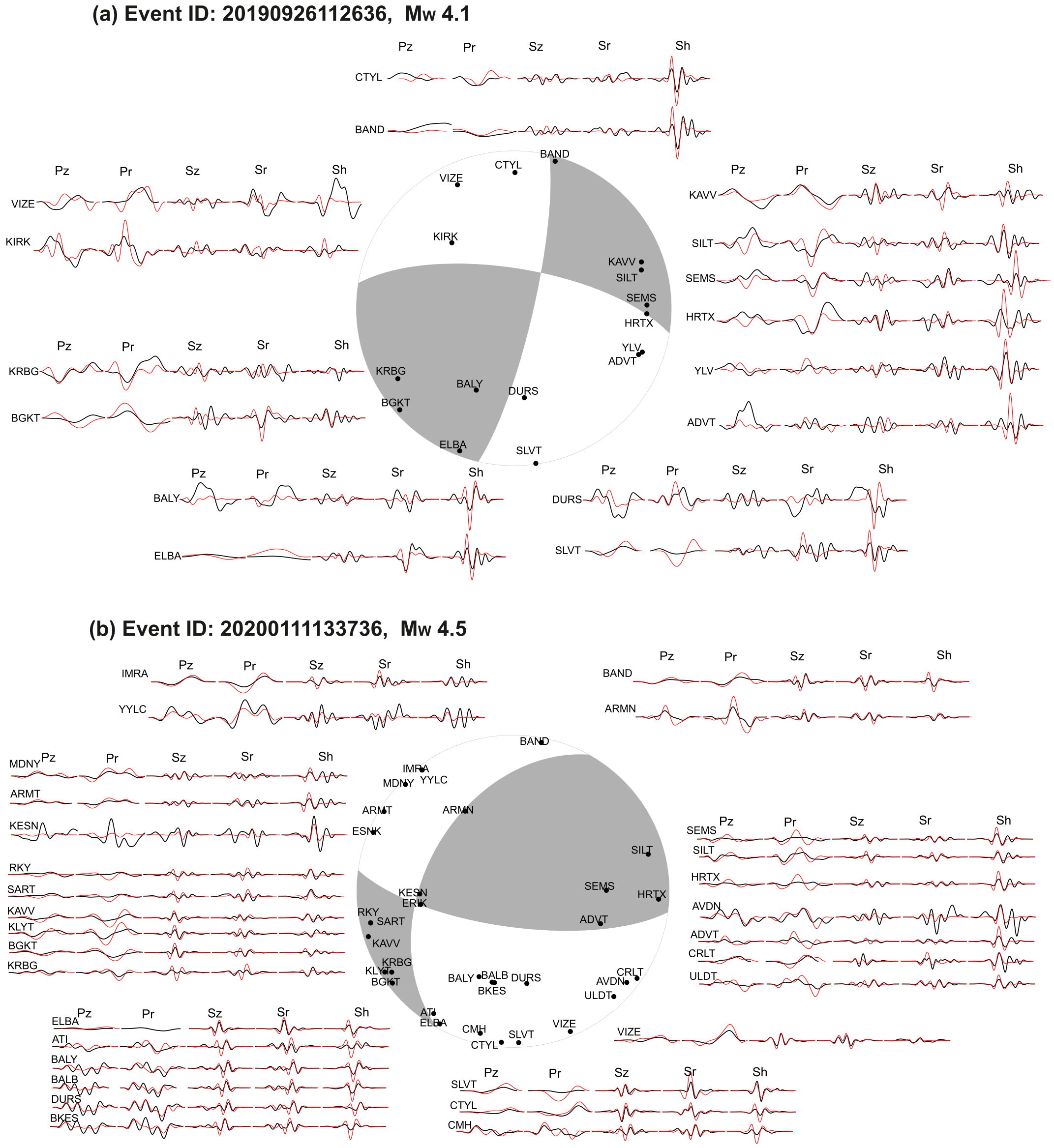

Figure 3. Source mechanism inversion results and waveform fittings for two representative earthquakes. (a) Focal mechanism of event 20190926112636 with M_L 4.4 that occurred on fault segment CB (cf. Figure 1) with strike = 279°, dip = 69°, and rake = 169°. Observed waveform segments (black) and model fitting (red) are shown for vertical (Pz), radial (Pr), vertical surface wave (Sz), radial surface wave (Sr), and tangential surface wave (Sh) components at different stations. (b) Focal mechanism of M_L 4.9 event 20200111133736 that occurred on KB segment with strike = 98°, dip = 71°, and rake = 130°.

strike-slip source mechanisms, mainly showing near vertical faults striking ~94 ± 8° NE. Source mechanisms of 14 earthquakes were estimated in the eastern side of the Central Basin toward the Kumburgaz Basin (CBe-KB), where earthquakes show strike-slip faulting and a set of nodal planes trend in east–south direction with an average strike of 99°. In the eastern part of the Cinarcık Basin (CE), five earthquakes show large variations in strike directions and a larger normal-faulting component. Here, the main fault trace splits into the northern and middle branches bounding the Cinarcık basin, and a shear-zone consisting of multiple normal faults is present within the basin. Hence, this variability could be due to the activation of different sets of faults. In addition to events along the MMF, two normal-faulting earthquakes are observed in the off-fault region along the sub-branch (Figure 4a).

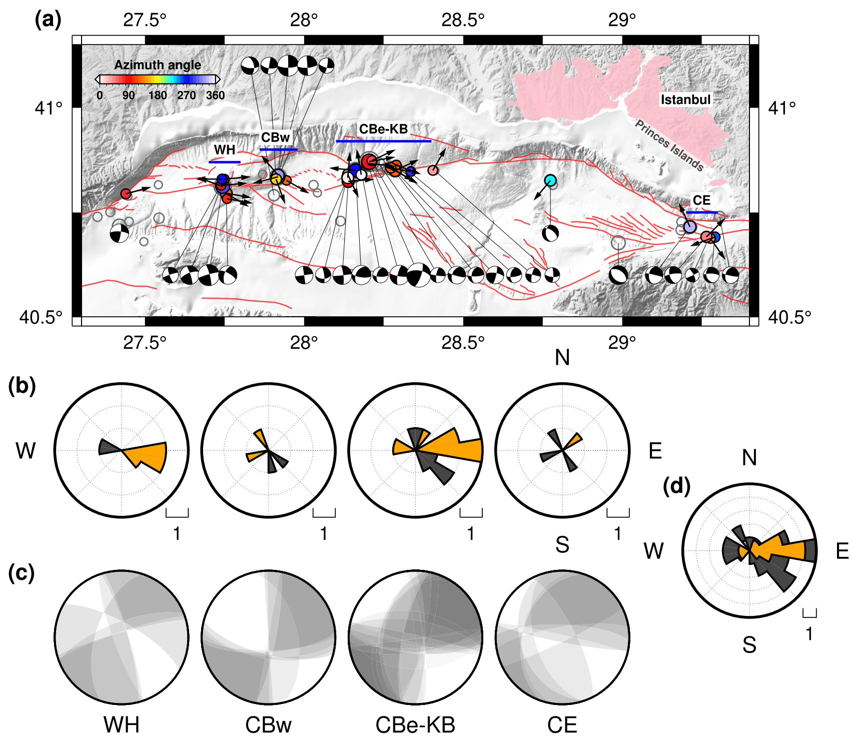

Figure 4. Preferred orientations of earthquake rupture directivity using unilateral and asymmetric bilateral models for $M_L \geq 3.5$ earthquakes along the MMF. (a) Surface distribution of rupture directivity orientations and source mechanisms. Circles show the resolved $M_L \geq 3.5$ earthquakes with color coding and arrows indicating the azimuthal angle of rupture direction. Blue lines highlight the four clusters analyzed in (b, c). (b) Rose diagrams of obtained earthquake rupture directions per cluster. Superposed yellow rose diagrams show the unilateral directivity results that pass the *t*-test. (c) Source mechanisms superposed for the events belonging to the clusters correspondingly. (d) Rose diagram of preferential rupture directions for all analyzed earthquakes.

3.2. Rupture Directivity Orientation Consistent With Fault Strike

Utilizing the EGF deconvolution and ASTF analysis at different azimuths, we resolve the earthquake rupture directivity for 31 events with $M_L \geq 3.5$ (see three examples in Figures 2b–2f), among which 25 also have source mechanisms derived in this study. The obtained rupture directivity parameters for individual earthquakes are provided in Table S2 of Supporting Information S1.

We first employ a pure unilateral model (Equation 1) to constrain the rupture directivity. Of the analyzed events, 17 display a preferred eastward rupture propagation with θ between 30° and 120°; in the opposite direction, 8 earthquakes display westward rupture propagation with θ within $(220°, 320°)$. The remaining earthquakes show best fitting directions departing from the E–W trending direction of MMF.

For the estimated rupture directivities from the unilateral model, we further conduct a two-sample *t*-test to check the significance of ASTF variation in the forward and backward directions (Text S3 in Supporting Information S1). 18 out of the 31 earthquakes passed the *t*-test, suggesting that ASTF duration differences are statistically significant in the two directions and the rupture propagation shows a strong asymmetry (Figure S2 in Supporting Information S1). This includes the three events shown in Figure 2. Among the 18 strongly asymmetric events, 13 (72%) show a first-order eastward rupture with θ in the range 30°–120°, while the other 5 earthquakes (28%) show θ ranging from 220° to 320°. We note that events with constrained directivity inconsistent with the fault strike are rejected by the *t*-test, while the rupture directivity of remaining events follows the E–W fault trending direction. For the 13 remaining events that did not pass the *t*-test, we applied bilateral rupture models (Equation 2) to fit the ASTF variation (Figure S3 in Supporting Information S1). Introducing an additional parameter χ improved the fitting, while no dramatic changes occurred to the rupture direction. 3 out of 13 events show slight dominant eastward ruptures, and another 3 show a weak dominant direction toward the west; 7 earthquakes show either a bilateral pattern or a weak dominant direction departing from the E–W trend.

Combining the unilateral and asymmetric bilateral ruptures, earthquakes displaying preferred eastward rupture propagation show a median rupture direction of $\theta = 85°$, close to the azimuth of the MMF at this region, which is ~80° up to the Istanbul Bend (at 28.8° Longitude) (Figure 4a). A second trend of rupture directions appears at about $\theta = 140°$ with weak asymmetric ruptures, being approximately orthogonal to the main fault trace and likely associated with the conjugate structures (Figure 4d). This orientation is mostly, but not exclusively, observed at the edges of the CBe and CBw.

We analyze the preferential rupture orientations at selected segments of the MMF by grouping the seismicity according to spatial clusters (Figure 4). The WH cluster includes 7 rupture directivity estimations, out of which 5 show strong eastward ruptures and the other two events show weak westward propagation. Earthquakes in the CBw are located at the edge of the CB, where faults consist of multiple sub-branches. Here, 3 out of 4 rupture directions align along a northwest-southeast direction, which could be related to the mapped local faults bounding the basin or the stress distribution from basin effects. Almost half of the total events are located within the CBe-KB. Out of the 14 analyzed events from this cluster, 9 display preferential rupture directivities with $\theta = 30°–120°$. Most of them occurred during the 2019 Silivri sequence that culminated with a M_L 5.7 earthquake and display a rupture directivity trending around $\theta = 75°$ (Figure 4c). In the CE, earthquake directivities from 5 events show larger variations as well as source mechanisms. This could be attributed to the presence of complex fault systems with different orientations.

Using the directivity models (Equations 1 and 2), we also resolved the rupture velocity V_r and rupture length L. The estimated V_r values show a large variation from 10% to 90% V_S with a median value of $V_r = 30\%\ V_S$, and the L values range from 0.1 to 2 km with a weak correlation with the M_L. The relatively low V_r and small L values are not uncommon in rupture directivity calculations (e.g., Abercrombie et al., 2017; Prieto et al., 2017; Ross & Ben-Zion, 2016) and should be regarded as "effective." One possible origin is the potential earthquake rupture complexity of EGF events, which is not an ideal point source and will affect deconvolution results of target events. Since the L and V_r are not as well constrained as the θ, we do not further interpret them and instead focus only on analyzing the obtained earthquake rupture direction in this study. In addition, we further tested a different model to fit the ASTF durations (Calderoni et al., 2020, following Ben-Menahem, 1961; Boatwright, 2007) and obtained similar results for the unilateral and strong asymmetric ruptures; see details in Text S4, Figure S4 and Table S3 of Supporting Information S1.

4. Discussion

Rupture directivity provides key information for seismic hazard and risk assessment that can be gained by analyzing the earthquake source. In the following, we compare our observations with those from other well-resolved moderate-magnitude earthquake sequences, elaborate on the potential mechanisms driving rupture directivity at this study area, and discuss the implications for ground shaking near the Istanbul Metropolitan region.

4.1. Comparison With Rupture Directivity From Other Similar Tectonic Settings

While there is a scarce number of studies resolving earthquake rupture directivity properties on the MMF, rupture directivities for small to moderate earthquakes have been resolved in other continental transform plate boundaries. One of the best studied strike-slip environments is the San Andreas Fault (SAF) system in California. For the SAF creeping segment, rupture directivity patterns have been analyzed through spectral ratio for M0.5–3.0 events (Wang & Rubin, 2011) and displacement spectra comparison for $M > 3$ earthquakes (Kane et al., 2013). A southeast direction was observed to be the preferred earthquake rupture directivity, which is consistent with predictions from the resolved velocity contrast across the fault (Rubin, 2002; Rubin & Gillard, 2000). A similar rupture directivity orientation was resolved for the southern San Jacinto fault from measuring and modeling peak ground motions (Kurzon et al., 2014), consistent with the surface fault trace and predictions from measured velocity contrasts along the fault. Along-strike preferential orientation is not only a characteristic feature of strike-slip boundaries, but it has also been observed to be a main factor controlling the rupture directivity along the Apennine Mountain Chain in Italy (e.g., Calderoni et al., 2015, 2017).

Our results provide the first rupture directivity estimations for small to medium-sized earthquakes along this offshore portion of the MMF, together with previous estimations from the ground motion of specific earthquakes such as the 2019 M_L 5.7 Silivri (Türker et al., 2022). As the last $M > 6$ earthquake along the MMF occurred in

1963, no detailed instrumental information from rupture directivity of large earthquakes is available. Information about rupture directivity from large earthquakes during the instrumental period may be combined with geological evidence supporting directivity effects of historical earthquakes (e.g., Dor et al., 2006; Wechsler et al., 2009). Unfortunately, geological inferences are difficult in this offshore portion of the MMF, and any asymmetry in seismicity distribution across the fault is difficult to observe due to the presence of sedimentary basins. The derived results can be augmented by analyzing additional signals that may reflect rupture directivity such as along-strike asymmetry of aftershocks (e.g., Calderoni et al., 2023; Zaliapin & Ben-Zion, 2011). Such work requires a separate dedicated analysis and is left for a future study.

4.2. Mechanisms Driving the Preferred Rupture Direction

Several physical mechanisms can give rise to a preferential earthquake rupture directivity along a fault segment. As summarized by Calderoni et al. (2015), such mechanisms may encompass (a) complexities in the fault geometry, which may enhance propagation toward the direction with reduced normal stress; (b) aseismic deformation leading to a persistent stress gradient that encourages earthquake rupture propagation toward regions experiencing a stress increase; (c) crustal wave channeling in particular directions due to phenomena such as coupling with basin waveguides; (d) fluid dynamics effects; and (e) the presence of bimaterial fault interfaces that facilitate preferential propagation in the direction corresponding to the motion of the side characterized by lower seismic velocity at depth.

With the current analysis, we can resolve the orientations of preferential rupture directivity along the MMF, but only hypothesize about which of the mechanism(s) mentioned above may most prominently contribute to the observed eastward rupture directivity in the MMF. The western portion of the MMF appears to be partially creeping (Bohnhoff, Wollin, et al., 2017; Schmittbuhl et al., 2016; Yamamoto et al., 2019), while east of the central basin there is a transition to a fully locked status (Becker et al., 2023a; Bohnhoff et al., 2013; Ergintav et al., 2014). In this respect, as the coupling of the fault increases toward the east, so does the stress accumulated on the fault, hence creating a stress gradient toward the east which may favor the earthquake propagation in this direction.

Another possibility is a velocity contrast across the fault, forming a bimaterial interface that could promote the occurrence of eastward rupture directivity. Theoretical and laboratory studies indicate that rupture directivity on bimaterial interfaces tend to propagate toward the direction of motion of the more compliant block (lower seismic velocity) at depth (Ampuero & Ben-Zion, 2008; Andrews & Ben-Zion, 1997; Ben-Zion & Shi, 2005; Shlomai & Fineberg, 2016; Weertman, 1980). Seismological approaches to identify a velocity contrast across a fault include tomographic imaging (e.g., Allam & Ben-Zion, 2012; Ozakin et al., 2012; Thurber et al., 2006) and analysis of fault-zone head waves that refract along bimaterial interfaces (e.g., Ben-Zion, 1990; Bulut et al., 2012; Najdahmadi et al., 2016; Share & Ben-Zion, 2016). However, so far neither of the two approaches has yet unambiguously identified a velocity contrast across the MMF (e.g., Yamamoto et al., 2022). If our observations are governed by the existence of a bimaterial interface, the theoretical expectations for bimaterial ruptures suggest that the slower side of the MMF should be the northern block. Detailed near-fault observations would be needed to verify this hypothesis in the future.

4.3. Implications for Future Large Earthquakes Near Istanbul and Associated Ground Motion

Classic ground-motion prediction equations (GMPEs) used in engineering seismology typically assume an isotropic spatial distribution and azimuthal-dependent features are generally not included. In recent years, the effect of earthquake directivity on ground-motion prediction has been considered in various studies (e.g., Somerville et al., 1997; Spudich & Chiou, 2008; Spudich et al., 2013; Weatherill & Lilienkamp, 2023). However, implementing directivity effects requires knowledge of the dominant earthquake rupture directivity patterns in the specific regions. Hence, the resolved earthquake directivity in this study provides valuable information for seismic hazard and risk assessments in the Istanbul metropolitan region.

Our results indicate a preference of rupture propagation toward the East on the western and central MMF. This suggests that ground shaking might be comparatively larger toward the Istanbul Metropolitan region in a systematic way. In this regard, our results are consistent with a previous directivity estimation for the 2019 M_L 5.7 Silivri earthquake in the central MMF from ground-motion analysis (Turker et al., 2022).

Assuming that rupture directivity of smaller events can be resolved reliably, an important open question is whether rupture directivity resolved from smaller events in the MMF can be upscaled to the large events that occur periodically along the NAFZ. Smaller events sample local seismogenic environments, while the rupture process of large earthquakes can be affected by other factors like nucleation location (Martínez-Garzón & Poli, 2024), variant seismogenic width along the fault (Weng & Yang, 2017), and structural complexities. The presence of bimaterial interfaces or stress gradients may promote a more unilateral rupture over selected fault sections, regardless of the magnitude of the corresponding event. Moreover, for bimaterial ruptures, the effect of the velocity contrast on rupture propagation increases with the propagation distance (e.g., Adams, 1995; Ben-Zion & Huang, 2002; Brietzke & Ben-Zion, 2006), so preferred directivity of small events on a bimaterial interface would be amplified for large earthquakes. Unfortunately, the rupture directivity in the central and western part of the MMF pointing eastwards may result in enhancing the ground shaking toward Istanbul. This suggests that, to generate more realistic seismic hazard and risk models for the Istanbul Metropolitan region, it may be important to consider eastward directivity effects.

5. Conclusions

We resolved for the first time earthquake rupture directivity patterns for 31 moderate ($3.5 \leq M_L \leq 5.7$) earthquakes along the MMF segment of the North Anatolian Fault, near the Istanbul megalopolis. To that end, we derived robust source mechanisms by waveform modeling and analyzed the earthquake directivity using the azimuthal distribution of earthquake ASTFs.

Our reliable source mechanisms indicate a predominance of strike-slip kinematics, which is consistent with the geological traces of the central and western portions of the MMF, in contrast with a larger proportion of normal faulting in Western Marmara reported in previous studies inverting first-motion polarities.

Over half of the analyzed earthquakes display a predominant rupture direction trending eastwards around 85°, indicating consistency with the strike of the MMF. Within the strong asymmetric events, the proportion of eastward rupture is 72%, and the westward propagation takes up 28%.

According to these results, earthquake ground shaking may be statistically more pronounced toward the Istanbul metropolitan region. Including such frequent eastward directivity effects toward the Istanbul metropolitan region can impact estimates of seismic hazard assessment for the region.

Data Availability Statement

The continuous waveforms from this study were downloaded from the websites of different agencies including KOERI (Kandilli Observatory And Earthquake Research Institute, Boğaziçi University, 1971, http://www.koeri.boun.edu.tr/sismo/2/data-request/, last accessed 05/07/2024), AFAD (Disaster and Emergency Management Authority, 1990, https://tdvms.afad.gov.tr/continuous_data, last accessed 05/07/2024), GONAF (Bohnhoff, Dresen, et al., 2017, https://geofon.gfz-potsdam.de/waveform/archive/network.php?ncode=GF, last accessed 05/07/2024) and PIRES (GFZ Potsdam, BU-Kandilli, 2006; Bohnhoff et al., 2013, https://geofon.gfz-potsdam.de/waveform/archive/network.php?ncode=PZ, last accessed 05/07/2024) networks. The spectra for target events and EGFs in this study are provided in Chen, Martínez-Garzón et al. (2024). The catalog employed in this study is published in a data service publication (Becker et al., 2023b). MATLAB and Generic Mapping Tools (Wessel et al., 2019) are used for data processing and figure producing.

Acknowledgments

The study benefited from discussions with Massimo Cocco, Dirk Becker, Dino Bindi and Georg Dresen. We thank Giovanna Calderoni, an anonymous reviewer, and Editor German Prieto for constructive comments that helped us to improve the manuscript. X.C. was supported by the Deutsche Forschungs Gemeinschaft (DFG) in the frame of the ICDP-SPP proposal “Earthquake source characterization and directivity effects near Istanbul: Implications for seismic hazard.” P.M.G. acknowledges funding from the ERC Starting Grant -101076119 (QUAKEHUNTER).

References

Abercrombie, R. E., Poli, P., & Bannister, S. (2017). Earthquake directivity, orientation, and stress drop within the subducting plate at the Hikurangi Margin, New Zealand: Directivity of New Zealand earthquakes. *Journal of Geophysical Research: Solid Earth*, *122*(12), 10176–10188. https://doi.org/10.1002/2017JB014935

Adams, G. G. (1995). Self-excited oscillations of two elastic half-spaces sliding with a constant coefficient of friction. *Journal of Applied Mechanics*, *62*(4), 867–872. https://doi.org/10.1115/1.2896013

Allam, A. A., & Ben-Zion, Y. (2012). Seismic velocity structures in the southern California plate-boundary environment from double-difference tomography. *Geophysical Journal International*, *190*(2), 1181–1196. https://doi.org/10.1111/j.1365-246X.2012.05544.x

Ambraseys, N. (2002). The seismic activity of the Marmara sea region over the last 2000 years. *Bulletin of the Seismological Society of America*, *92*(1), 1–18. https://doi.org/10.1785/0120000843

Ampuero, J.-P., & Ben-Zion, Y. (2008). Cracks, pulses and macroscopic asymmetry of dynamic rupture on a Bimaterial interface with velocity-weakening friction. *Geophysical Journal International*, *173*(2), 674–692. https://doi.org/10.1111/j.1365-246X.2008.03736.x

Andrews, D. J., & Ben-Zion, Y. (1997). Wrinkle-like slip pulse on a fault between different materials. *Journal of Geophysical Research*, *102*(B1), 553–571. https://doi.org/10.1029/96JB02856

Becker, D., Martínez-Garzón, P., Wollin, C., Kılıç, T., & Bohnhoff, M. (2023a). Variation of fault creep along the overdue Istanbul-Marmara seismic gap in NW Türkiye. *Geophysical Research Letters*, *50*(6), e2022GL101471. https://doi.org/10.1029/2022GL101471

Becker, D., Martínez-Garzón, P., Wollin, C., Kılıç, T., & Bohnhoff, M. (2023b). Homogenized regional seismicity catalogue for the Marmara region, northwestern Turkey, for the time interval 2006–2020. V. 1.0 [Dataset]. *GFZ Data Services*. https://doi.org/10.5880/GFZ.4.2.2023.002

Ben-Menahem, A. (1961). Radiation of seismic surface-waves from finite moving sources. *Bulletin of the Seismological Society of America*, *51*(3), 401–435. https://doi.org/10.1785/BSSA0510030401

Ben-Menahem, A., & Singh, S. J. (1981). *Seismic waves and sources*. Springer. https://doi.org/10.1007/978-1-4612-5856-8

Ben-Zion, Y. (1990). The response of two half spaces to point dislocations at the material interface. *Geophysical Journal International*, *101*, 507–528.

Ben-Zion, Y., & Huang, Y. (2002). Dynamic rupture on an interface between a compliant fault zone layer and a stiffer surrounding solid. *Journal of Geophysical Research*, *107*(B2). https://doi.org/10.1029/2001JB000254

Ben-Zion, Y., & Shi, Z. (2005). Dynamic rupture on a material interface with spontaneous generation of plastic strain in the bulk. *Earth and Planetary Science Letters*, *236*(1–2), 486–496. https://doi.org/10.1016/j.epsl.2005.03.025

Boatwright, J. (2007). The persistence of directivity in small earthquakes. *Bulletin of the Seismological Society of America*, *97*(6), 1850–1861. https://doi.org/10.1785/0120050228

Boatwright, J., & Boore, D. M. (1982). Analysis of the ground accelerations radiated by the 1980 Livermore Valley earthquakes for directivity and dynamic source characteristics. *Bulletin of the Seismological Society of America*, *72*(6A), 1843–1865. https://doi.org/10.1785/BSSA07206A1843

Bohnhoff, M., Bulut, F., Dresen, G., Malin, P. E., Eken, T., & Aktar, M. (2013). An earthquake gap south of Istanbul. *Nature Communications*, *4*(1), 1999. https://doi.org/10.1038/ncomms2999

Bohnhoff, M., Dresen, G., Ceken, U., Kadirioglu, F. T., Kartal, R. F., Kilic, T., et al. (2017). GONAF-The borehole geophysical observatory at the North Anatolian Fault in the eastern Sea of Marmara. *Scientific Drilling*, *22*, 19–28. https://doi.org/10.5194/sd-22-19-2017

Bohnhoff, M., Martínez-Garzón, P., Bulut, F., Stierle, E., & Ben-Zion, Y. (2016). Maximum earthquake magnitudes along different sections of the North Anatolian fault zone. *Tectonophysics*, *674*, 147–165. https://doi.org/10.1016/j.tecto.2016.02.028

Bohnhoff, M., Wollin, C., Domigall, D., Küperkoch, L., Martínez-Garzón, P., Kwiatek, G., et al. (2017). Repeating Marmara sea earthquakes: Indication for fault creep. *Geophysical Journal International*, *210*(1), 332–339. https://doi.org/10.1093/gji/ggx169

Brietzke, G. B., & Ben-Zion, Y. (2006). Examining tendencies of in-plane rupture to migrate to material interfaces. *Geophysical Journal International*, *167*(2), 807–819. https://doi.org/10.1111/j.1365-246X.2006.03137.x

Bulut, F., Ben-Zion, Y., & Bohnhoff, M. (2012). Evidence for a Bimaterial interface along the Mudurnu segment of the North Anatolian Fault Zone from polarization analysis of P waves. *Earth and Planetary Science Letters*, *327–328*, 17–22. https://doi.org/10.1016/j.epsl.2012.02.001

Calderoni, G., Di Giovambattista, R., & Ventura, G. (2023). A reliable procedure to estimate the rupture propagation directions from source directivity: The 2016–2018 Central Italy seismic sequence. *Seismological Research Letters*, *94*(4), 1912–1924. https://doi.org/10.1785/0220220318

Calderoni, G., Gervasi, A., La Rocca, M., & Ventura, G. (2020). Strike-slip earthquakes at the Northern edge of the Calabrian arc subduction zone. *Seismological Research Letters*, *92*(2A), 1023–1035. https://doi.org/10.1785/0220200251

Calderoni, G., Rovelli, A., Ben-Zion, Y., & Di Giovambattista, R. (2015). Along-strike rupture directivity of earthquakes of the 2009 L'Aquila, central Italy, Seismic sequence. *Geophysical Journal International*, *203*(1), 399–415. https://doi.org/10.1093/gji/ggv275

Calderoni, G., Rovelli, A., & Di Giovambattista, R. (2017). Rupture directivity of the strongest 2016–2017 Central Italy earthquakes. *Journal of Geophysical Research: Solid Earth*, *122*(11), 9118–9131. https://doi.org/10.1002/2017JB014118

Cesca, S., Heimann, S., & Dahm, T. (2011). Rapid directivity detection by azimuthal amplitude spectra inversion. *Journal of Seismology*, *15*(1), 147–164. https://doi.org/10.1007/s10950-010-9217-4

Chen, X., Kwiatek, G., Bindi, D., Becker, D., Bohnhoff, M., Cotton, F., & Martínez-Garzón, P. (2024b). Stress-Drop variations of (A)seismic fault segments in the Sea of Marmara region (Northwestern Türkiye) supported by different methodological approaches. *Bulletin of the Seismological Society of America*, 1–15. https://doi.org/10.1785/0120240128

Chen, X., Martínez-Garzón, P., Kwiatek, G., Ben-zion, Y., Bohnhoff, M., & Cotton, F. (2024a). Spectra for 31 M_L ≥3.5 earthquakes in the Sea of Marmara region, Türkiye, during 2006–2020 [Dataset]. *GFZ Data Services*. https://doi.org/10.5880/GFZ.4.2.2024.003

Chen, Y., Letort, J., Cotton, F., & Drouet, S. (2014). High-frequency directivity effects: Evidence from analysis of the les Saintes records. *Journal of Seismology*, *18*(3), 457–466. https://doi.org/10.1007/s10950-014-9419-2

Colavitti, L., Lanzano, G., Sgobba, S., Pacor, F., & Gallovič, F. (2022). Empirical evidence of frequency-dependent directivity effects from small-to-moderate normal fault earthquakes in Central Italy. *Journal of Geophysical Research: Solid Earth*, *127*(6), e2021JB023498. https://doi.org/10.1029/2021JB023498

Disaster and Emergency Management Authority. (1990). Turkish national seismic network [Dataset]. *Department of Earthquake, Disaster and Emergency Management Authority*. https://doi.org/10.7914/SN/TU

Dor, O., Rockwell, T. K., & Ben-Zion, Y. (2006). Geological observations of damage asymmetry in the structure of the San Jacinto, san Andreas and punchbowl faults in southern California: A possible indicator for preferred rupture propagation direction. *Pure and Applied Geophysics*, *163*(2–3), 301–349. https://doi.org/10.1007/s00024-005-0023-9

Durand, V., Bentz, S., Kwiatek, G., Dresen, G., Wollin, C., Heidbach, O., et al. (2020). A two-scale preparation phase preceded an Mw 5.8 earthquake in the Sea of Marmara offshore Istanbul, Turkey. *Seismological Research Letters*, *91*(6), 3139–3147. https://doi.org/10.1785/0220200110

Ergintav, S., Reilinger, R. E., Çakmak, R., Floyd, M., Çakir, Z., Doğan, U., et al. (2014). Istanbul's earthquake hot spots: Geodetic constraints on strain accumulation along faults in the Marmara seismic gap. *Geophysical Research Letters*, *41*(16), 5783–5788. https://doi.org/10.1002/2014GL060985

GFZ Potsdam, BU-Kandilli. (2006). Prince Islands real-time earthquake monitoring system [Dataset]. *International Federation of Digital Seismograph Networks*. https://doi.org/10.7914/SN/PZ

Hartzell, S. H. (1978). Earthquake aftershocks as Green's functions. *Geophysical Research Letters*, *5*(1), 1–4. https://doi.org/10.1029/GL005i001p00001

He, X., Ni, S., & Liu, J. (2015). Rupture directivity of the August 3rd, 2014 Ludian earthquake (Yunan, China). *Science China Earth Sciences*, *58*(5), 795–804. https://doi.org/10.1007/s11430-015-5053-2

Holmgren, J. M., Kwiatek, G., & Werner, M. J. (2023). Nonsystematic rupture directivity of geothermal energy induced microseismicity in Helsinki, Finland. *Journal of Geophysical Research: Solid Earth*, *128*(3), e2022JB025226. https://doi.org/10.1029/2022JB025226

Kandilli Observatory And Earthquake Research Institute, Boğaziçi University. (1971). Kandilli Observatory and Earthquake Research Institute (KOERI) [Dataset]. *International Federation of Digital Seismograph Networks*. https://doi.org/10.7914/SN/KO

Kane, D. L., Shearer, P. M., Goertz-Allmann, B. P., & Vernon, F. L. (2013). Rupture directivity of small earthquakes at Parkfield. *Journal of Geophysical Research: Solid Earth*, *118*(1), 212–221. https://doi.org/10.1029/2012JB009675

Karabulut, H., Schmittbuhl, J., Özalaybey, S., Lengliné, O., Kömeç-Mutlu, A., Durand, V., et al. (2011). Evolution of the seismicity in the eastern Marmara sea a decade before and after the 17 August 1999 Izmit earthquake. *Tectonophysics*, *510*(1–2), 17–27. https://doi.org/10.1016/j.tecto.2011.07.009

Kurzon, I., Vernon, F. L., Ben-Zion, Y., & Atkinson, G. (2014). Ground motion prediction equations in the San Jacinto fault Zone: Significant effects of rupture directivity and Fault Zone Amplification. *Pure and Applied Geophysics*, *171*(11), 3045–3081. https://doi.org/10.1007/s00024-014-0855-2

Kwiatek, G. (2008). Relative source time functions of seismic events at the Rudna copper mine, Poland: Estimation of inversion uncertainties. *Journal of Seismology*, *12*(4), 499–517. https://doi.org/10.1007/s10950-008-9100-8

Lange, D., Kopp, H., Royer, J.-Y., Henry, P., Çakir, Z., Petersen, F., et al. (2019). Interseismic strain build-up on the submarine North Anatolian fault offshore Istanbul. *Nature Communications*, *10*(1), 3006. https://doi.org/10.1038/s41467-019-11016-z

Lengliné, O., & Got, J.-L. (2011). Rupture directivity of microearthquake sequences near Parkfield, California. *Geophysical Research Letters*, *38*(8), L08310. https://doi.org/10.1029/2011GL047303

López-Comino, J. Á., Cesca, S., Niemz, P., Dahm, T., & Zang, A. (2021). Rupture directivity in 3D inferred from acoustic emissions events in a mine-scale Hydraulic fracturing experiment. *Frontiers in Earth Science*, *9*. https://doi.org/10.3389/feart.2021.670757

Malin, P. E., Bohnhoff, M., Blümle, F., Dresen, G., Martínez-Garzón, P., Nurlu, M., et al. (2018). Microearthquakes preceding a M4.2 earthquake offshore Istanbul. *Scientific Reports*, *8*(1), 16176. https://doi.org/10.1038/s41598-018-34563-9

Martínez-Garzón, P., Becker, D., Jara, J., Chen, X., Kwiatek, G., & Bohnhoff, M. (2023). The 2022 MW 6.0 Gölyaka–Düzce earthquake: An example of a medium-sized earthquake in a fault Zone early in its seismic cycle. *Solid Earth*, *14*(10), 1103–1121. https://doi.org/10.5194/se-14-1103-2023

Martínez-Garzón, P., & Poli, P. (2024). Cascade and pre-slip models oversimplify thecomplexity of earthquake preparation in nature. *Communications Earth & Environment*, *5*(1), 120. https://doi.org/10.1038/s43247-024-01285-y

McGuire, J. J. (2004). Estimating finite source properties of small earthquake ruptures. *Bulletin of the Seismological Society of America*, *94*(2), 377–393. https://doi.org/10.1785/0120030091

Meng, H., McGuire, J. J., & Ben-Zion, Y. (2020). Semiautomated estimates of directivity and related source properties of small to moderate southern California earthquakes using second seismic moments. *Journal of Geophysical Research: Solid Earth*, *125*(4), e2019JB018566. https://doi.org/10.1029/2019JB018566

Murru, M., Akinci, A., Falcone, G., Pucci, S., Console, R., & Parsons, T. (2016). M $\geq$ 7 earthquake rupture forecast and time-dependent probability for the Sea of Marmara region, Turkey. *Journal of Geophysical Research: Solid Earth*, *121*(4), 2679–2707. https://doi.org/10.1002/2015JB012595

Najdahmadi, B., Bohnhoff, M., & Ben-Zion, Y. (2016). Bimaterial interfaces at the Karadere segment of the North Anatolian fault, Northwestern Turkey. *Journal of Geophysical Research: Solid Earth*, *121*(2), 2015JB012601. https://doi.org/10.1002/2015JB012601

Ozakin, Y., Ben-Zion, Y., Aktar, M., Karabulut, H., & Peng, Z. (2012). Velocity contrast across the 1944 rupture zone of the North Anatolian fault east of Ismetpasa from analysis of Teleseismic arrivals. *Geophysical Research Letters*, *39*(8). https://doi.org/10.1029/2012GL051426

Öztürk, Y. K., Özel, N. M., & Özbakir, A. D. (2015). States of local stresses in the Sea of Marmara through the analysis of large numbers of small earthquakes. *Tectonophysics*, *665*, 37–57. https://doi.org/10.1016/j.tecto.2015.09.027

Parsons, T. (2004). Recalculated probability of M $\geq$ 7 earthquakes beneath the Sea of Marmara, Turkey. *Journal of Geophysical Research*, *109*(B5), B05304. https://doi.org/10.1029/2003JB002667

Prieto, G. A., Froment, B., Yu, C., Poli, P., & Abercrombie, R. (2017). Earthquake rupture below the brittle-ductile transition in continental lithospheric mantle. *Science Advances*, *3*(3), e1602642. https://doi.org/10.1126/sciadv.1602642

Prieto, G. A., Shearer, P. M., Vernon, F. L., & Kilb, D. (2004). Earthquake source scaling and self-similarity estimation from stacking P and S spectra. *Journal of Geophysical Research*, *109*(B8), B08310. https://doi.org/10.1029/2004JB003084

Ross, Z. E., & Ben-Zion, Y. (2016). Toward reliable automated estimates of earthquake source properties from body wave spectra. *Journal of Geophysical Research: Solid Earth*, *121*(6), 4390–4407. https://doi.org/10.1002/2016JB013003

Rubin, A. M. (2002). Aftershocks of microearthquakes as probes of the mechanics of rupture. *Journal of Geophysical Research*, *107*(B7), 2142. https://doi.org/10.1029/2001JB000496J

Rubin, A. M., & Gillard, D. (2000). Aftershock asymmetry/rupture directivity among central San Andreas fault microearthquakes. *Journal of Geophysical Research*, *105*(B8), 19095–19109. https://doi.org/10.1029/2000jb900129

Schmittbuhl, J., Karabulut, H., Lengliné, O., & Bouchon, M. (2016). Seismicity distribution and locking depth along the main Marmara Fault, Turkey. *Geochemistry, Geophysics, Geosystems*, *17*(3), 954–965. https://doi.org/10.1002/2015GC006120

Seekins, L. C., & Boatwright, J. (2010). Rupture directivity of moderate earthquakes in Northern California. *Bulletin of the Seismological Society of America*, *100*(3), 1107–1119. https://doi.org/10.1785/0120090161

Seo, M., Kim, W., & Kim, Y. (2022). Rupture directivity of the 2021 ML 2.2 Gwangyang, Korea, microearthquake: Toward resolving high-resolution rupture process of a small earthquake. *The Seismic Record*, *2*(4), 227–236. https://doi.org/10.1785/0320220030

Share, P.-E., & Ben-Zion, Y. (2016). Bimaterial interfaces in the south san Andreas Fault with opposite velocity contrasts NW and SE from San Gorgonio pass. *Geophysical Research Letters*, *43*(20), 2016GL070774. https://doi.org/10.1002/2016GL070774

Shlomai, H., & Fineberg, J. (2016). The structure of slip-pulses and supershear ruptures driving slip in Bimaterial friction. *Nature Communications*, *7*(1), 11787. https://doi.org/10.1038/ncomms11787

Somerville, P. G., Smith, N. F., Graves, R. W., & Abrahamson, N. A. (1997). Modification of empirical strong ground motion attenuation relations to include the amplitude and duration effects of rupture directivity. *Seismological Research Letters*, *68*(1), 199–222. https://doi.org/10.1785/gssrl.68.1.199

Spudich, P., Bayless, J. R., Baker, J. W., Chiou, B. S. J., Rowshandel, B., Shahi, S. K., & Somerville, P. (2013). *Final report of the NGA-West2 directivity working Group. (PEER Report; Vol. 2013/09)*. Pacific Earthquake Engineering Research Center (PEER).

Spudich, P., & Chiou, B. S. J. (2008). Directivity in NGA earthquake ground motions: Analysis using Isochrone theory. *Earthquake Spectra*, *24*(1), 279–298. https://doi.org/10.1193/1.2928225

Tan, Y., & Helmberger, D. (2010). Rupture directivity characteristics of the 2003 big bear sequence. *Bulletin of the Seismological Society of America*, *100*(3), 1089–1106. https://doi.org/10.1785/0120090074

Thurber, C., Zhang, H., Waldhauser, F., Hardebeck, J., Michael, A., & Eberhart-Phillips, D. (2006). Three-dimensional compressional wavespeed model, earthquake relocations, and focal mechanisms for the Parkfield, California, region. *Bulletin of the Seismological Society of America*, *96*(4B), S38–S49. https://doi.org/10.1785/0120050825

Tibi, R., Bock, G., Xia, Y., Baumbach, M., Grosser, H., Milkereit, C., et al. (2001). Rupture processes of the 1999 August 17 Izmit and November 12 Düzce (Turkey) earthquakes. *Geophysical Journal International*, *144*(2), F1–F7. https://doi.org/10.1046/j.1365-246x.2001.00360.x

Tinti, E., Scognamiglio, L., Michelini, A., & Cocco, M. (2016). Slip heterogeneity and directivity of the ML 6.0, 2016, Amatrice earthquake estimated with rapid finite-fault inversion. *Geophysical Research Letters*, *43*(20), 10745–10752. https://doi.org/10.1002/2016GL071263

Turhan, F., Acarel, D., Plicka, V., Bohnhoff, M., Polat, R., & Zahradník, J. (2023). Coseismic faulting complexity of the 2019 Mw 5.7 Silivri earthquake in the central Marmara seismic Gap, offshore Istanbul. *Seismological Research Letters*, *94*(1), 75–86. https://doi.org/10.1785/0220220111

Türker, E., Cotton, F., Pilz, M., & Weatherill, G. (2022). Analysis of the 2019 Mw 5.8 Silivri earthquake ground motions: Evidence of systematic azimuthal variations associated with directivity effects. *Seismological Research Letters*, *93*(2A), 693–705. https://doi.org/10.1785/0220210168

Türker, E., Yen, M., Pilz, M., & Cotton, F. (2023). Significance of pulse-like ground motions and directivity effects in moderate earthquakes: The example of the Mw 6.1 Gölyaka-Düzce earthquake on 23 November 2022. *Bulletin of the Seismological Society of America*, *114*(2), 955–964. https://doi.org/10.1785/0120230043

Venkataraman, A., & Kanamori, H. (2004). Observational constraints on the fracture energy of subduction zone earthquakes. *Journal of Geophysical Research*, *109*(B5). https://doi.org/10.1029/2003JB002549

Wang, C. Y., & Herrmann, R. B. (1980). A numerical study of P-SV-and SH-wave generation in a plane layered medium. *Bulletin of the Seismological Society of America*, *70*(4), 1015–1036. https://doi.org/10.1785/BSSA0700041015

Wang, E., & Rubin, A. M. (2011). Rupture directivity of microearthquakes on the San Andreas Fault from spectral ratio inversion. *Geophysical Journal International*, *186*(2), 852–866. https://doi.org/10.1111/j.1365-246X.2011.05087.x

Weatherill, G., & Lilienkamp, H. (2023). Capturing directivity in probabilistic seismic hazard analysis for New Zealand: Challenges, implications, and a machine learning approach for implementation. *Bulletin of the Seismological Society of America*, *114*(1), 373–398. https://doi.org/10.1785/0120230161

Wechsler, N., Rockwell, T. K., & Ben-Zion, Y. (2009). Application of high resolution DEM data to detect rock damage from geomorphic signals along the central San Jacinto Fault. *Geomorphology*, *113*(1), 82–96. https://doi.org/10.1016/j.geomorph.2009.06.007

Weertman, J. (1980). Unstable slippage across a fault that separates elastic media of different elastic constants. *Journal of Geophysical Research*, *85*(B3), 1455–1461. https://doi.org/10.1029/JB085iB03p01455

Weng, H., & Yang, H. (2017). Seismogenic width controls aspect ratios of earthquake ruptures. *Geophysical Research Letters*, *44*(6), 2725–2732. https://doi.org/10.1002/2016GL072168

Wessel, P., Luis, J. F., Uieda, L., Scharroo, R., Wobbe, F., Smith, W. H. F., & Tian, D. (2019). The generic mapping Tools version 6. *Geochemistry, Geophysics, Geosystems*, *20*(11), 5556–5564. https://doi.org/10.1029/2019GC008515

Wollin, C., Bohnhoff, M., Martínez-Garzón, P., Küperkoch, L., & Raub, C. (2018). A unified earthquake catalogue for the Sea of Marmara Region, Turkey, based on automatized phase picking and travel-time inversion: Seismotectonic implications. *Tectonophysics*, *747–748*, 416–444. https://doi.org/10.1016/j.tecto.2018.05.02

Wollin, C., Bohnhoff, M., Vavryčuk, V., & Martínez-Garzón, P. (2019). Stress inversion of regional seismicity in the Sea of Marmara region, Turkey. *Pure and Applied Geophysics*, *176*(3), 1269–1291. https://doi.org/10.1007/s00024-018-1971-1

Yamamoto, R., Kido, M., Ohta, Y., Takahashi, N., Yamamoto, Y., Pinar, A., et al. (2019). Seafloor geodesy revealed partial creep of the North Anatolian fault submerged in the Sea of Marmara. *Geophysical Research Letters*, *46*(3), 1268–1275. https://doi.org/10.1029/2018GL080984

Yamamoto, Y., Kalafat, D., Pinar, A., Takahashi, N., Polat, R., Kaneda, Y., & Ozener, H. (2022). Seismic velocity structure along the North Anatolian fault beneath the central Marmara sea and its implication for seismogenesis. *Geophysical Journal International*, *228*(1), 396–411. https://doi.org/10.1093/gji/ggab351

Yoshida, K., Saito, T., Emoto, K., Urata, Y., & Sato, D. (2019). Rupture directivity, stress drop, and hypocenter migration of small earthquakes in the Yamagata-Fukushima border swarm triggered by upward pore-pressure migration after the 2011 Tohoku-Oki earthquake. *Tectonophysics*, *769*, 228184. https://doi.org/10.1016/j.tecto.2019.228184

Zaliapin, I., & Ben-Zion, Y. (2011). Asymmetric distribution of aftershocks on large faults in California. *Geophysical Journal International*, *185*(3), 1288–1304. https://doi.org/10.1111/j.1365-246X.2011.04995.x

Zhang, Y., Tang, X., Liu, D., Taymaz, T., Eken, T., Guo, R., et al. (2023). Geometric controls on cascading rupture of the 2023 Kahramanmaraş earthquake doublet. *Nature Geoscience*, *16*(11), 1054–1060. https://doi.org/10.1038/s41561-023-01283-3

Zhao, L.-S., & Helmberger, D. V. (1994). Source estimation from broadband regional seismograms. *Bulletin of the Seismological Society of America*, *84*(1), 91–104. https://doi.org/10.1785/BSSA0840010091

Zhu, L., & Helmberger, D. V. (1996). Advancement in source estimation techniques using broadband regional seismograms. *Bulletin of the Seismological Society of America*, *86*(5), 1634–1641. https://doi.org/10.1785/BSSA0860051634

Zhu, L., & Rivera, L. A. (2002). A note on the dynamic and static displacements from a point source in multilayered media. *Geophysical Journal International*, *148*(3), 619–627. https://doi.org/10.1046/j.1365-246X.2002.01610.x

References From the Supporting Information

Bentz, S., Martínez-Garzón, P., Kwiatek, G., Bohnhoff, M., & Renner, J. (2018). Sensitivity of full moment tensors to data preprocessing and inversion parameters: A case study from the Salton sea geothermal FieldSensitivity of FMT to data preprocessing and inversion parameters: A case study from the SSGF. *Bulletin of the Seismological Society of America*, *108*(2), 588–603. https://doi.org/10.1785/0120170203

Domański, B., Gibowicz, S. J., & Wiejacz, P. (2002). Source time function of seismic events at Rudna copper mine, Poland. In C. I. Trifu (Ed.), *The mechanism of Induced seismicity* (pp. 131–144). Birkhäuser. https://doi.org/10.1007/978-3-0348-8179-1_6

Kwiatek, G., Plenkers, K., & Dresen, G., & JAGUARS Research Group. (2011). Source parameters of Picoseismicity recorded at mponeng deep gold mine, South Africa: Implications for scaling relations. *Bulletin of the Seismological Society of America*, *101*(6), 2592–2608. https://doi.org/10.1785/0120110094

Li, Y., Doll, C., Jr., & Toksöz, M. N. (1995). Source characterization and fault plane determination for MbLg = 1.2 to 4.4 earthquakes in the charlevoix seismic zone, Quebec, Canada. *Bulletin of the Seismological Society of America*, *85*(6), 1604–1621. https://doi.org/10.1785/BSSA0850061604

Velasco, A. A., Ammon, C. J., & Lay, T. (1994). Empirical green function deconvolution of broadband surface waves: Rupture directivity of the 1992 Landers, California (Mw = 7.3), earthquake. *Bulletin of the Seismological Society of America*, *84*(3), 735–750. https://doi.org/10.1785/BSSA0840030735

Warren, L. M., & Silver, P. G. (2006). Measurement of differential rupture durations as constraints on the source finiteness of deep-focus earthquakes. *Journal of Geophysical Research*, *111*(B6). https://doi.org/10.1029/2005JB004001